Master of Science Thesis

Quantum Optics in 2D Nonlinear Lattices

Katarina Stensson

Quantum Electronics and Quantum Optics
Department of Applied Physics
School of Engineering Sciences
Royal Institute of Technology, SE-106 91 Stockholm, Sweden

Stockholm, Sweden 2014

Typeset in LaTeX

Examensarbete inom ämnet Kvantoptik för avläggande av civilingenjörsexamen inom utbildningsprogrammet Teknisk Fysik.

Graduation thesis on the subject Quantum Optics for the degree of Master of Science in Engineering from the School of Engineering Physics.

TRITA-FYS 2014:32
ISSN 0280-316X
ISRN KTH/FYS/–14:32–SE

Printed in Sweden by Universitetsservice US AB, Stockholm 2014

Abstract

In this work the properties of light produced by spontaneous parametric down-conversion (SPDC) in 2D nonlinear lattices have been studied. A quantum mechanical model of 2D SPDC was formulated, solved in the general case, and analyzed in the special case when two different signals are coupled as a consequence of their idlers being degenerate in frequency and spatial propagation. According to the model these 'twin signals' are correlated in phase and amplitude, and the gain coefficient of the coupled processes enhanced by a factor $\sqrt{2}$. The analytically derived correlations and the gain enhancement was supported experimentally by measurements on a hexagonal lattice in a $LiTaO_3$ crystal.

Acknowledgements

I would like to thank my supervisor Katia Gallo for her enthusiasm and encouragements, and for letting me explore the lab, often by myself. It did not always go the way I wanted, but I have definitely learned a lot! Thanks also to Gunnar Björk for interesting discussions.

Contents

Chapter 1

Introduction

During the last two decades there has been a growing interest in harnessing quantum mechanical effects for new types of technologies. This interest have led to increased importance of understanding quantum states of light, and how to manipulate and produce such states. In research today, sources creating entangled photon states are an essential tool for a great variety of fundamental quantum optical experiments, such as testing Bell-inequalities[1, 2], precise phase measurement [3, 4], and realizing quantum networks [5] or quantum teleportation [6]. Significant efforts are directed towards practical quantum information processing [7, 8, 9], where integrated light sources would allow for e.g. compact on-chip entangled pair production, improving multifunction, stability and portability.

Nonlinear optics has proven to provide a way to create different kinds of entangled photon states. Especially the quasi phase matching (QPM) technique, first introduced in a pioneering paper on frequency conversion by Armstrong & Bloembergen [10], allow efficient photon production through spontaneous parametric down-conversion (SPDC), with great spectral flexibility [11, 12]. Achieving phase matching by modulating the nonlinear susceptibility periodically in one dimension is now a standard technique. 1D QPM structures are well understood and have developed into a wide variety of innovative optical devices[13, 14].

The technique for periodic poling of ferroelectric domains in nonlinear materials has been very successful since it was first experimentally realized in the beginning of the nineties [11]. Since Berger suggested extending the 1D QPM technique to multiple dimensions in 1998 [15], 2D QPM structures have emerged as a way to obtain even larger spectral and spatial flexibility. In 2D QPM structures the sign of the nonlinear susceptibility $\chi^{(2)}$ is reversed periodically in two spatial dimensions, granting access to a larger parameter space [16]. By domain engineering in two dimensions, spatial and temporal properties of entangled photons can be controlled during QPM SPDC, resulting in new types of photon entanglement[17]. These entangled states, produced by SPDC in two-dimensional nonlinear lattices, will be investigated throughout this work.

In 2D structures the down-conversion efficiency is generally lower than in one dimensional QPM, although coupled interaction between two SPDC processes can substantially increase the parametric gain, approaching the 1D case [18]. This 'locking' of two distinct resonances of the 2D lattice is done by two SPDC processes

sharing a common idler, and results in a pair of signal beams at the output, generated simultaneously and emitted symmetrically around the symmetry axis of the crystal. The spectral and spatial flexibility of SPDC by 2D QPM can allow for steering between different types of entanglement, by varying geometrical and experimental parameters, and thereby shift the balance between resonances [16]. Also, by enabling entanglement in both the frequency, spatial and polarization domain, some researchers have suggested 2D QPM structures as a means to approach the idea of hyperentanglement over several degrees of freedom [17].

Although the possibilities to make use of 2D QPM structures for quantum optics applications are overwhelming, studies on the subject are few, and there remains a lot to be explored. In this work the focus is on investigating the quantum mechanical properties of light produced by spontaneous parametric down-conversion (SPDC) in two dimensional quasi phase matched (2D QPM) nonlinear crystals. The coupled interactions, where two signals share a common idler (or vice versa), is of special interest. By analytic means the quantum mechanical correlations in phase and amplitude of the coupled interactions have been investigated, including their dependency on the degree of 'sharing', or overlap, of the idler(s). Furthermore, this work demonstrates gain enhancement and amplitude correlations of coupled SPDC processes, by measurements on a hexagonally poled MgO-doped $LiTaO_3$ substrate (hexMgSLT).

Aim

The aim of this thesis is to better understand the behavior of light produced by SPDC in a 2D quasi phase matched crystal. The possibilities of the many types of quantum correlations and entanglement involved in this process are not yet explored. This work will shed some light on certain aspects of 2D QPM processes and the properties of the produced light, particularly the case when two SPDC processes are coupled. The work presented in this thesis is a basis for further investigation of entangled state production by SPDC in 2D QPM lattices, towards novel applications in emerging quantum based technologies.

Outline

The text is organized as follows. Chapter 2 contains the theoretical background. It introduces the main concepts and the framework for the theoretical and experimental investigations. In Chapter 3 a quantum mechanical model of 2D SPDC is formulated, from which solutions are derived, and analyzed for the shared idler case. Chapter 4 contains the numerical and experimental work, including a description of the preparatory work, experimental procedure and measurement results. The investigation and the results are further discussed in Chapter 5, while Chapter 6 contains concluding remarks.

Abbreviations

Abbreviation	Description
PDC	Parametric Down-Conversion
SPDC	Spontaneous Parametric Down-Conversion
OPG	Optical Parametric Generation
OPA	Optical Parametric Amplification
2D	Two Dimensional
QPM	Quasi Phase Matching
SS	Shared Signal
SI	Shared Idler
SLT	Stoichiometric Lithium Tantalate
hexMgSLT	Hexagonally poled, MgO-doped SLT

Chapter 2

Theoretical background

2.1 Parametric down-conversion

To achieve generation of entangled photon states using nonlinear photonic crystals, one will deal with the so called parametric processes, or more precisely, the process of parametric down-conversion (PDC). In down-conversion, one photon incident on a nonlinear medium breaks up into new photons of lower frequencies. Nonlinear parametric processes spur from the nonlinear part of the polarization induced in the medium by an incoming electromagnetic field. The polarization can be expanded in a Taylor series in the electric field $\mathbf{E}$.

$$\mathbf{P} = \epsilon_0 \chi^{(1)} \mathbf{E} + \mathbf{P}^{NL} = \epsilon_0 \left[\chi^{(1)} \mathbf{E} + \chi^{(2)} \mathbf{E}\mathbf{E} + \chi^{(3)} \mathbf{E}\mathbf{E}\mathbf{E} + O(\mathbf{E}^4) \right]$$

Where $\chi^{(n)}$ is the rank $n+1$ (electric) susceptibility tensor. The terms decrease in strength with n, so that the higher order contributions are negligible and the first non-zero nonlinear term will be dominating nonlinear interaction. For non-centrosymmetric materials, i.e materials lacking a center of symmetry, both even and odd orders in the expansion are non-zero, and $\chi^{(2)}$ will be the dominating term. A more thorough description of the origin and behavior of parametric nonlinear interactions can be found in textbooks [19, 20].

In $\chi^{(2)}$ processes, three modes are interacting under the condition of energy and momentum conservation. Assuming monochromatic plane waves, this condition can be expressed as

$$\omega_p = \omega_s + \omega_i \tag{2.1}$$

$$\mathbf{k}_p = \mathbf{k}_s + \mathbf{k}_i \tag{2.2}$$

Where ω denotes frequency and $\mathbf{k}$ is the wavevector (the linear momentum is $p = \hbar k$). The incoming frequency ω_p is referred to as the *pump* frequency, while ω_s and ω_i are known as the *signal* and *idler* frequencies, in order of decreasing energy.

There exists different kinds of $\chi^{(2)}$ down-conversion processes, as shown in figure 2.1. In difference frequency generation (DFG), pump and signal interact to produce a wave at the lower frequency $\omega_i = \omega_p - \omega_s$. In optical parametric amplification (OPA), the signal is amplified by energy transfer from the pump. At the same time

an idler is also produced and equivalently amplified. The process is shown in the middle in figure 2.1. The physics behind the two processes are the same, but they differ from an application point of view, and in the relative strength of pump and signal at the input.

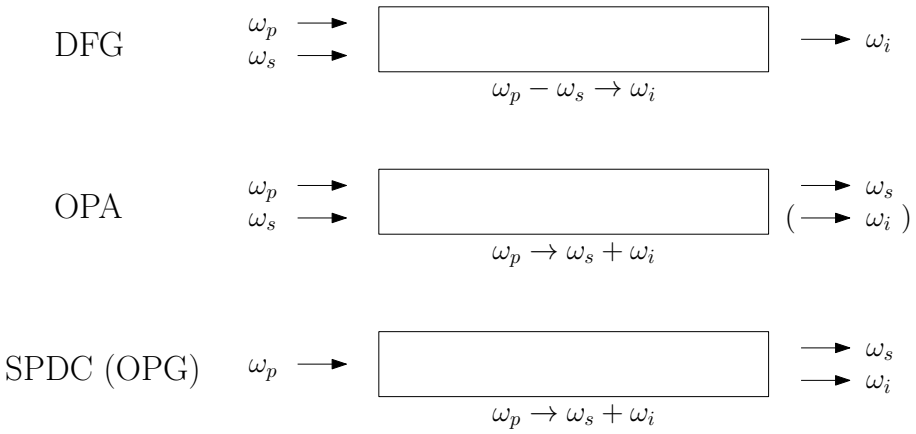

Figure 2.1: Illustration of three kinds of $\chi^{(2)}$ PDC processes: difference frequency generation (DFG), optical parametric amplification (OPA) and spontaneous parametric down-conversion (SPDC, also known as optical parametric generation, OPG). In down-conversion processes, energy is transferred from the pump field to the signal and/or idler fields at lower frequencies.

The process which will be the focus of this work is known as either optical parametric generation (OPG) or spontaneous parametric down-conversion (SPDC). The term SPDC will be used in the following. SPDC is different from DFG and OPA in the sense that only the pump wave is present at the input. The generation of signal and idler is stimulated by vacuum fluctuations in the nonlinear medium, and is thus a quantum mechanical phenomenon. The effect was first studied by Kleinman in 1968, at that time referred to as optical parametric noise [21].

2.2 Quantum mechanical description of SPDC

Spontaneous parametric down-conversion, based on $\chi^{(2)}$ nonlinearities being three-mode processes, can be described by three creation and annihilation operators. The Hamiltonian, representing the quantum mechanical energy state of the system, can be written in the following form.

$$\hat{H} = \hat{H}_0 + \hat{H}_{int} = \sum_{m=p,s,i} \hbar\omega_m \left(\hat{n}_m + \frac{1}{2}\right) + \hbar\kappa' \left[\hat{a}_s^\dagger \hat{a}_i^\dagger \hat{a}_p + h.c\right] \tag{2.3}$$

The first part of the Hamiltonian in eq. 2.3 represents the energy present in the electromagnetic field modes of frequency ω_p, ω_s and ω_i. The interaction part of the Hamiltonian describes the interaction - annihilation of a photon at frequency ω_p, and simultaneous creation of two photons at frequencies ω_s and ω_i. The opposite

process is described by the hermitian conjugate $h.c.$ The strength of the process is determined by the coupling constant κ'.

Suppose the pump beam is much more intense than the generated beams at frequencies ω_i and ω_s. Then the pump can be considered a classical field with constant amplitude. This is called the no pump-depletion approximation, and is valid as long as the conversion efficiency is low. By assuming this is true, and the conditions in eq. 2.1 and 2.2 satisfied, looking at the interaction picture, i.e. applying the rotating wave approximation, we write:

$$\hat{H}_{int} = \hbar\kappa \left[\hat{a}_s^\dagger \hat{a}_i^\dagger + h.c.\right] \tag{2.4}$$

where the pump amplitude has been incorporated in the coupling constant $\kappa = \kappa' a_p(0)$. The time evolution of the system is governed by the Heisenberg equation of motion, written for any hermitian operator $\hat{O}$ as

$$\frac{d}{dt}\hat{O}(t) = \frac{i}{\hbar}\left[\hat{H}(t), \hat{O}(t)\right] \tag{2.5}$$

For the signal $\hat{a}_s(t)$ and the idler $\hat{a}_i(t)$ the equations of motion take the form

$$\begin{aligned} \frac{d\hat{a}_s(t)}{dt} &= -i\kappa\hat{a}_i^\dagger \\ \frac{d\hat{a}_i(t)}{dt} &= -i\kappa\hat{a}_s^\dagger \end{aligned} \tag{2.6}$$

By differentiating a second time, substituting and solving the now uncoupled equations for $\hat{a}_s$ and $\hat{a}_i$, with appropriate initial conditions $\hat{a}_s(0)$ and $\hat{a}_(0)$, the signal and idler creation and annihilation operators take the following form.

$$\begin{aligned} \hat{a}_s(t) &= \hat{a}_s(0)\cosh(\kappa t) + i\hat{a}_i^\dagger(0)\sinh(\kappa t) \\ \hat{a}_i(t) &= \hat{a}_i(0)\cosh(\kappa t) + i\hat{a}_s^\dagger(0)\sinh(\kappa t) \end{aligned} \tag{2.7}$$

Now the expectation values of idler and signal photon numbers can be calculated. Assuming the initial state of both signal and idler modes to be the vacuum state $|0_s, 0_i\rangle$, the expectation value for the signal follows.

$$\begin{aligned} \langle\hat{n}_s(t)\rangle =& \langle 0_s, 0_i|\hat{a}_s^\dagger(t)\hat{a}_s(t)|0_s, 0_i\rangle \\ =& \langle 0_s, 0_i|[\hat{a}_s^\dagger(0)\cosh(\kappa t) - i\hat{a}_i(0)\sinh(\kappa t)] \\ & \times [\hat{a}_s(0)\cosh(\kappa t) + i\hat{a}_i^\dagger(0)\sinh(\kappa t)]|0_s, 0_i\rangle \\ =& \sinh^2(\kappa t)\langle 0_s, 0_i|\hat{a}_i(0)\hat{a}_i^\dagger(0)|0_s, 0_i\rangle \\ =& \sinh^2(\kappa t)\langle 0_s, 0_i|(\hat{n}_i(0)+1)|0_s, 0_i\rangle \\ =& \sinh^2(\kappa t) \end{aligned} \tag{2.8}$$

The result for the idler is identical.

The intensity of the down-converted light is proportional to the expectation value of the photon number obtained in eq. 2.8. The relation between the creation and annihilation operators and the real physical system will be further discussed in section 2.3.

2.3 SPDC in a physical system

Realizing spontaneous parametric down-conversion in a physical system is a way to obtain photon states entangled in the frequency domain (and potentially other domains, such as polarization) like the case presented above. Different attempts to achieve SPDC in physical systems have been made, since the process was first explained in the sixties [21], using materials with suitable nonlinear properties. In the above discussions we assumed the momentum conservation condition in eq. 2.2 to be satisfied. This is not the general case for electromagnetic waves propagating in nonlinear media, since dispersion, i.e. the refractive index' dependency on frequency, is always present, and will cause the down-converted light to travel with a different phase velocity than the pump. Dispersion results in the inability to satisfy both energy (eq.2.1) and momentum (eq.2.2) conservation at once, which is usually represented by the momentum mismatch $\Delta\mathbf{k}$.

$$\Delta\mathbf{k} = \mathbf{k}_p - \mathbf{k}_s - \mathbf{k}_i \tag{2.9}$$

To illustrate the effect of the momentum mismatch, one can look at the coupled wave equations, which can be seen as the analogue of the quantum mechanical equations of motion (eq. 2.6) in classical electromagnetic theory. If we again assume the conversion efficiency to be low, and thus the pump field non-depleted so that $A_p(x) \simeq A_p(0)$, the coupled wave equations describing the SPDC can be written in the following way [19].

$$\begin{aligned} \frac{dA_s(x)}{dx} &= -i\gamma_s A_p(0) A_i^*(x) e^{-i\Delta k x} \\ \frac{dA_i(x)}{dx} &= -i\gamma_i A_p(0) A_s^*(x) e^{-i\Delta k x} \end{aligned} \tag{2.10}$$

assuming monochromatic plane waves so that A_m is the complex field amplitude according to $E_m = A_m(x)e^{ik_m x}$. The coordinate x is the distance traveled in the nonlinear medium. The individual coupling constants γ_s and γ_i are given by $\gamma_m = \frac{\omega_m\sqrt{\mu_0\epsilon_0}}{n_m}d$, where n_m is the index of refraction and d is related to the nonlinear susceptibility $\chi^{(2)}$. Let us normalize the fields by making the substitution

$$A_m = \sqrt{\frac{\omega_m}{n_m}}a_m \tag{2.11}$$

so that a_m physically represents the photon flux amplitude. The individual coupling constants γ_s, γ_i can be transformed into one single coupling parameter,

which we will denote κ for now. Now, assuming perfect phase matching $\Delta k = 0$, the coupled wave equations become

$$\begin{aligned} \frac{da_s(x)}{dx} &= -i\kappa a_i^*(x) \\ \frac{da_i(x)}{dx} &= -i\kappa a_s^*(x) \end{aligned} \tag{2.12}$$

and by comparing equations 2.10 and 2.12, identification gives an expression for the coupling constant κ.

$$\begin{aligned} A_p(0)\gamma_i &= \sqrt{\frac{n_s\omega_i}{n_i\omega_s}}\kappa \\ A_p(0)\gamma_s &= \sqrt{\frac{n_i\omega_s}{n_s\omega_i}}\kappa \end{aligned} \tag{2.13}$$

We can directly recognize the similarities of equation 2.12 with the equation of motion for signal and idler in eq. 2.6. This implies that the creation and annihilation operators are closely related to the normalized amplitudes of the electromagnetic field.

According to the coupled wave equations in eq. 2.10, the behavior of the signal and idler amplitudes is sinusoidal, with a period determined by $\Delta\mathbf{k}$. As a consequence there is no consequent build-up of signal and idler intensities. For $\Delta\mathbf{k}$=0, the intensities would instead evolve as $\sinh^4 \kappa x$, as given by eq. 2.8. For $\kappa t \ll 1$ the behavior is quadratic in κt, and in the limit $\kappa t \gg 1$ the intensity grows exponentially.

To obtain efficient down-conversion, ultimately exponential growth as predicted in eq. 2.8, one has to achieve *phase matching*, i.e. let $\Delta\mathbf{k} \simeq 0$. There are traditionally two ways of doing this. In *birefringent phase matching*, one exploits the fact that some crystals have a refractive index that is not only a function of the frequency, but also a function of the polarization of the propagating field, a property known as birefringence. Choosing different polarizations and incidence directions for the interacting fields, one can by means of birefringence compensate for the phase mismatch caused by dispersion.

An alternative technique is called *quasi phase matching* (QPM), first suggested in 1962 [10] but not really practically available until 1993 [11]. QPM does not fully compensate for the dispersion, but it allows a positive net flow of energy from the pump field to the signal and idler fields, by making sure the signal and idler are never more than 180 degrees out of phase with the pump. This is usually achieved by creating a periodic structure in the nonlinear crystal, and by that changing the sign of the nonlinear susceptibility $\chi^{(2)}$ with a certain periodicity, matching $2\pi/\Delta k$.

In ferroelectric materials the sign of the second order susceptibility is determined by the polarity, i.e the orientation of the spontaneous polarization, of the ferroelectric domains in the material. The spontaneous polarization can be locally reversed by application of an electric field, also known as electric-field poling, which can be used to obtain a QPM structure.

For experimentalists it is often convenient to use another form of the nonlinear susceptibility tensor $\chi^{(2)}$, namely the tensor $\mathbf{d} = \frac{1}{2}\chi^{(2)}$. The problem can be reduced to scalar form, for fixed polarizations. The tensor components of $\chi^{(2)}$ is then

expressed as the nonlinear coefficients d_{jkl}, where j, k, l denotes the polarization of the three fields involved in the interaction. Throughout this work we will be dealing with fields polarized along the z-axis of the crystal, and thus the nonlinear coefficient d_{33} will be used.

$$d_{33} = d_{zzz} = \frac{1}{2}\chi^{(2)}_{zzz} \tag{2.14}$$

An advantage of the QPM technique is that one can often exploit the largest nonlinear coefficient d, not being restricted to directions that satisfy the conditions for birefringent phase matching. The freedom of choosing the operational wavelengths might however be the greatest advantage of the QPM technique.

2.3.1 The QPM Principle

Implementing a QPM lattice in a nonlinear material implies changing the nonlinear coefficient d to a spatially varying function $d(x)$, periodic in x. The spatially varying function is written $d(x) = d_{33}f(x)$, where $f(x)$ is a dimensionless square wave modulation and varies from -1 to 1 with periodicity Λ. $f(x)$ can be decomposed to its Fourier components according to

$$d(x) = d_{33} \sum_{m=-\infty}^{\infty} F_m \exp(iG_m x) \tag{2.15}$$

where G_m is the momentum of the QPM lattice grating in the crystal, and relates to the grating period Λ through

$$G_m = \frac{2\pi}{\Lambda} m \tag{2.16}$$

m is an integer denoting the order of the Fourier decomposition. The Fourier coefficients are given by

$$F_m = \frac{1}{\Lambda} \int_0^{\Lambda} f(x) \exp(-iG_m x) dx \tag{2.17}$$

Inserting the Fourier decomposition of the susceptibility 2.15 into the coupled wave equations 2.10, most of the terms are fast oscillating and give negligible contributions to the overall signal and idler intensity build-up [22]. Only those terms satisfying $\Delta k \simeq G_m$, for a given QPM order m, will allow phase matching and contribute to efficient down-conversion. The condition for momentum or phase conservation in eq. 2.2 can in a quasi phase matched physical system then be replaced by the following QPM condition.

$$k_p - k_s - k_i - G_m = 0 \tag{2.18}$$

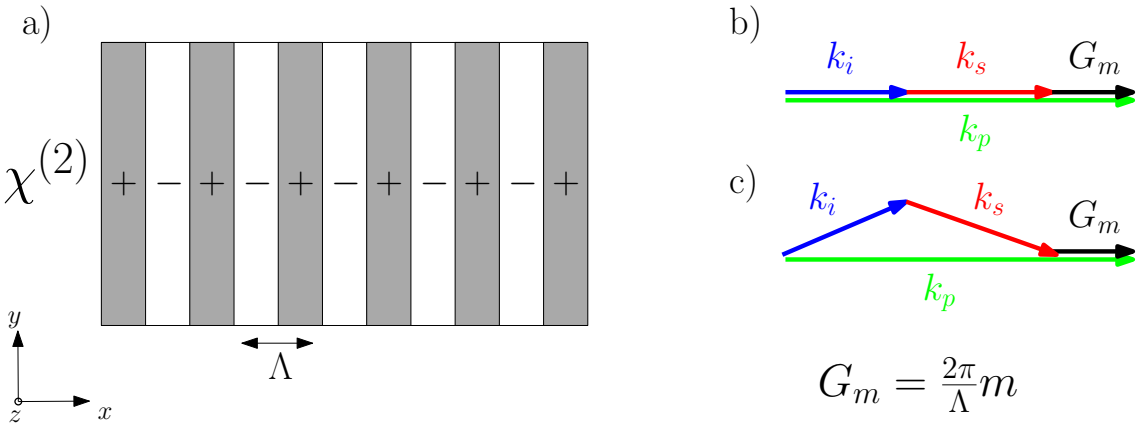

Figure 2.2: a)A QPM lattice periodically poled in the x-direction with grating period Λ. The nonlinear susceptibility switches between $+\chi^{(2)}$ and $-\chi^{(2)}$. To the right: momentum conservation illustrated by closing the diagram of wavevectors in the reciprocal lattice, for (b) signal and idler collinear with pump and (c) signal and idler propagating in directions different from the pump. The 'momentum of the grating' G makes up for the momentum mismatch Δk. In the non-collinear case one has to use the vector values of k_p, k_s, k_i and G_m.

The condition is illustrated in figure 2.2 for collinear and and non-collinear PDC in a one dimensional QPM lattice. In the non-collinear case, we have to take into account the vectorial form of eq. 2.18. The down-conversion process can now be described by the coupled wave equations as in eq. 2.10, with the momentum mismatch Δk substituted by the effective mismatch $\Delta k_{eff} = k_p - k_s - k_i - G_m \simeq 0$, and the nonlinear coefficient d changed to $d_{eff} = F_m d_{33}$. For the first order processes $F_m = \pi/2$ so that $d_{eff} = \frac{\pi}{2} d_{33}$.

2.3.2 Two-dimensional QPM

Achieving quasi phase matching by implementing a two-dimensional polarization-inverted structure (2D QPM) was first suggested by Berger in 1998 [15]. The 2D structure introduces new degrees of freedom in the spectral and angular response of nonlinear devices, allowing greater control during quasi phase matched down-conversion processes.

The principles for 2D QPM are similar to the 1D case, but the nonlinear coefficient d_{33} is now replaced by a function varying periodically in two spatial dimensions $d(x, y) = d_{33} f(x, y)$. To find the mathematical representation of the 2D QPM structure one can follow the derivations in [22]. For a hexagonal lattice, it results in reciprocal lattice vectors (RLV) $\mathbf{G}_{m,n}$, where the lowest order RLVs have magnitude

$$|\mathbf{G}| = \frac{4\pi}{\sqrt{3}\Lambda} \tag{2.19}$$

Possible two-dimensional periodic structures include hexagonal, square, rectangular, centered-rectangular and oblique lattices [22]. Figure 2.3 shows the real and reciprocal space of a hexagonal 2D lattice, which is what I will be focusing on in

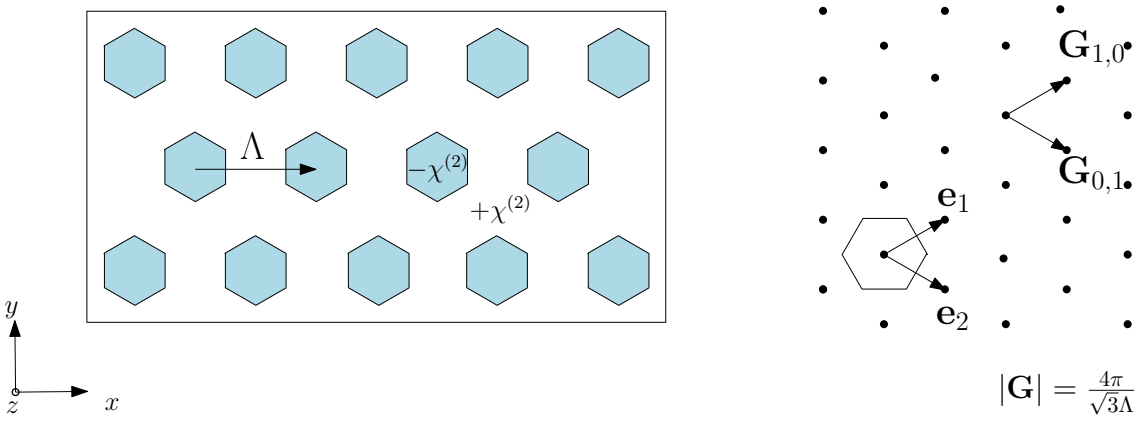

Figure 2.3: A hexagonal QPM grating with period Λ, for 2D QPM processes. The nonlinear susceptibility $\chi^{(2)}$ is periodically inverted. To the right: The reciprocal lattice of the hexagonal grating, with the hexagon at the bottom representing the 1^{st} Brillouin zone. The first order reciprocal lattice vectors (RLVs) $G_{1,0}$ and $G_{0,1}$ are shown.

the following, with the lowest order RLVs $G_{1,0}$ and $G_{0,1}$ from now on referred to as G_1 and G_2 respectively. G_1 and G_2 correspond to the basis vectors of the reciprocal space.

Because the Fourier coefficients of the two-dimensional spatially varying function $f(x, y)$ are smaller than in the 1D case (for the lowest order RLVs in a hexagonal lattice $F_{1,0} = F_{0,1} = \frac{3}{\pi^2}$), the efficiency for down-conversion in a 2D QPM lattice is also lower. However, the spatial and angular degrees of freedom allow for interesting possibilities lacking counterpart in 1D QPM geometries. Since the system of equations obtained from the QPM conditions 2.18 is underdetermined, the number of solutions is infinite for every RLV (see fig. 2.4 (a)). Which solutions are dominant in the SPDC process is instead determined by other factors. One example is when two solutions to the QPM conditions 2.18, i.e two different SPDC processes, utilizing 2 different RLVs to close the wavevector diagram, are degenerate in frequency and either idler or signal spatial propagation direction.

$$k_p - k_i - k_{s1} - G_1 = 0$$
$$k_p - k_i - k_{s2} - G_2 = 0$$

The situation can be described as the idler (or signal) being shared between two SPDC processes, as depicted in fig. 2.4 b). These two processes are then coherently coupled, leading to enhancement of these particular frequencies [17, 18].

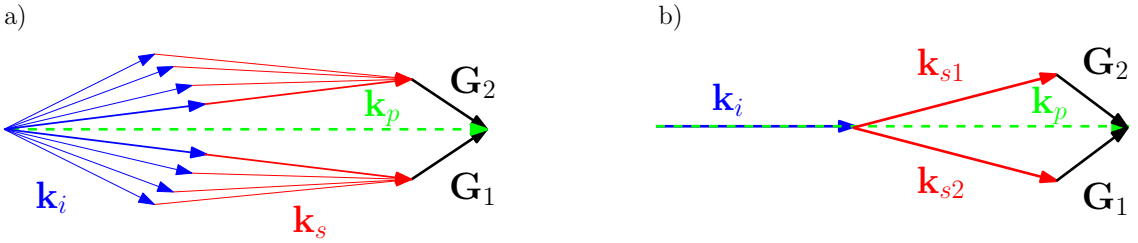

Figure 2.4: Momentum conservation in a two dimensional QPM structure is illustrated here by closing the wavevector diagram. a) In 2D QPM each reciprocal lattice vector $\mathbf{G}$ allow for an infinite number of solutions. b) for certain frequencies two different SPDC processes, utilizing two different RLVs, share a common idler (or signal). These particular frequencies are often enhanced because of coupling effects between the two processes.

Chapter 3

Quantum mechanical model of shared idler SPDC

When achieving SPDC in a two dimensional QPM structure, the 2D geometry can allow for two degenerate solutions to the QPM conditions, as explained in the end of section 2.3 The analytic model used here comprises 4 modes - two signals and two idlers. This is of course a simplification of reality, where a multitude of modes will interact. However, it will give a strong clue on the behavior of the down-converted light in the particular case that we are interested in, especially since the shared idler (shared signal) processes are dominant. The interaction Hamiltonian for the two signals and two idlers is presented in equation 3.1, where we let the two idlers overlap with a factor given by θ. For $\theta = 0$ the idlers are fully separated, for $\theta = \pi/2$, the idler is shared. The no pump depletion approximation is assumed to be valid, so the pump field is treated as a constant. The approximation is valid as long as the conversion efficiency is low, which is true for low pump powers. The interaction Hamiltonian is written as:

$$\begin{aligned}\hat{H}_{int} =& \hbar\kappa \left[\hat{a}_{s1}^{\dagger}\hat{a}_{i1}^{\dagger} + \hat{a}_{s1}\hat{a}_{i1}\right] + \hbar\kappa \left[\hat{a}_{s2}^{\dagger}\left(\cos\theta\hat{a}_{i2}^{\dagger} + \sin\theta\hat{a}_{i1}^{\dagger}\right) + \hat{a}_{s2}\left(\cos\theta\hat{a}_{i2} + \sin\theta\hat{a}_{i1}\right)\right] \\ =& \hbar\kappa \left[\hat{a}_{i1}^{\dagger}\left(\hat{a}_{s1}^{\dagger} + \sin\theta\hat{a}_{s2}^{\dagger}\right) + \hat{a}_{i1}\left(\hat{a}_{s1} + \sin\theta\hat{a}_{s2}\right) + \hat{a}_{i2}^{\dagger}\hat{a}_{s2}^{\dagger}\cos\theta + \hat{a}_{i2}\hat{a}_{s2}\cos\theta\right]\end{aligned} \tag{3.1}$$

Where $\hat{a}_{s1}$, $\hat{a}_{s2}$, $\hat{a}_{i1}$ and $\hat{a}_{i2}$ are the annihilation operators of the two signals and the two idlers respectively, and their hermitian conjugates are the corresponding creation operators.

Using the model described above, and the Schrödinger equation for time evolution in the Heisenberg picture

$$\frac{d\hat{a}(t)}{dt} = \frac{i}{\hbar}\left[\hat{H}, \hat{a}(t)\right]$$

we get the following differential equations.

$$\begin{aligned}
\frac{d\hat{a}_{i1}}{dt} =& i\kappa\left(\hat{a}^{\dagger}_{s1} + \sin\theta\hat{a}^{\dagger}_{s2}\right)\\
\frac{d\hat{a}_{i2}}{dt} =& i\kappa\cos\theta\hat{a}^{\dagger}_{s2}\\
\frac{d\hat{a}_{s1}}{dt} =& i\kappa\hat{a}^{\dagger}_{i1}\\
\frac{d\hat{a}_{s2}}{dt} =& i\kappa\left(\cos\theta\hat{a}^{\dagger}_{i2} + \sin\theta\hat{a}^{\dagger}_{i1}\right)
\end{aligned} \tag{3.2}$$

As shown in section 2.2 for a simpler case, the equations in 3.2 are related to the coupled wave equations in classic electromagnetic theory. By differentiating equations 3.2 a second time, these equations can be transformed into four 2^{nd} order differential equations for $\hat{a}_{i1}$, $\hat{a}_{i2}$, $\hat{a}_{s1}$ and $\hat{a}_{s2}$ that are still coupled in pairs. Differentiating a third time leads to four 4^{th} order equations, now uncoupled, presented here for $\hat{a}_{i1}$.

$$\frac{d^4\hat{a}_{i1}}{dt^4} - 2\kappa^2\frac{d^2\hat{a}_{i1}}{dt^2} + \kappa^4\cos^2\theta\hat{a}_{i1} = 0 \tag{3.3}$$

Equation 3.3 can be solved using the characteristic equation. With A,B,C and D constants that will be determined by initial conditions, the solution is

$$\begin{aligned}
\hat{a}_{i1}(t) = A\cosh(\kappa\sqrt{1+\sin\theta}t) + B\sinh(\kappa\sqrt{1+\sin\theta}t)\\
+ C\cosh(\kappa\sqrt{1-\sin\theta}t) + D\sinh(\kappa\sqrt{1-\sin\theta}t)
\end{aligned}$$

The original differential equations can now be used to find the expressions for the remaining operators. Writing the initial conditions as $\hat{a}_{i1}(0) = \hat{a}_{i10}$, $\hat{a}_{i2}(0) = \hat{a}_{i20}$, $\hat{a}_{s1}(0) = \hat{a}_{s10}$ and $\hat{a}_{s2}(0) = \hat{a}_{s20}$, the system can be solved and the constants A,B,C and D determined. The result is the following.

$$\begin{aligned}
A =& \frac{1}{2}\left[(1+\sin\theta)\hat{a}_{i10} + \cos\theta\hat{a}_{i20}\right]\\
B =& i\frac{\sqrt{1+\sin\theta}}{2}\left(\hat{a}^{\dagger}_{s10} + \hat{a}^{\dagger}_{s20}\right)\\
C =& \frac{1}{2}\left[(1-\sin\theta)\hat{a}_{i10} - \cos\theta\hat{a}_{i20}\right]\\
D =& i\frac{\sqrt{1-\sin\theta}}{2}\left(\hat{a}^{\dagger}_{s10} - \hat{a}^{\dagger}_{s20}\right)
\end{aligned}$$

Which finally gives the full expressions for the signal and idler creation and annihilation operators, for arbitrary overlap θ.

$$
\begin{aligned}
\hat{a}_{i1}(t) = &\frac{1}{2}\left[\left(1+\sin\theta\right)\hat{a}_{i10} + \cos\theta\hat{a}_{i20}\right]\cosh(\kappa\sqrt{1+\sin\theta}t) + \\
&+ \frac{i}{2}\sqrt{1+\sin\theta}\left(\hat{a}^{\dagger}_{s10} + \hat{a}^{\dagger}_{s20}\right)\sinh(\kappa\sqrt{1+\sin\theta}t) + \\
&+ \frac{1}{2}\left[\left(1-\sin\theta\right)\hat{a}_{i10} - \cos\theta\hat{a}_{i20}\right]\cosh(\kappa\sqrt{1-\sin\theta}t) + \\
&+ \frac{i}{2}\sqrt{1-\sin\theta}\left(\hat{a}^{\dagger}_{s10} - \hat{a}^{\dagger}_{s20}\right)\sinh(\kappa\sqrt{1-\sin\theta}t)
\end{aligned}
$$

$$
\begin{aligned}
\hat{a}_{i2}(t) = &\frac{1}{2}\left[\cos\theta\hat{a}_{i10} + \left(1-\sin\theta\right)\hat{a}_{i20}\right]\cosh(\kappa\sqrt{1+\sin\theta}t) + \\
&+ \frac{i}{2}\sqrt{1-\sin\theta}\left(\hat{a}^{\dagger}_{s10} + \hat{a}^{\dagger}_{s20}\right)\sinh(\kappa\sqrt{1+\sin\theta}t) + \\
&- \frac{1}{2}\left[\cos\theta\hat{a}_{i10} - \left(1+\sin\theta\right)\hat{a}_{i20}\right]\cosh(\kappa\sqrt{1-\sin\theta}t) + \\
&- \frac{i}{2}\sqrt{1+\sin\theta}\left(\hat{a}^{\dagger}_{s10} - \hat{a}^{\dagger}_{s20}\right)\sinh(\kappa\sqrt{1-\sin\theta}t)
\end{aligned}
$$

$$
\begin{aligned}
\hat{a}_{s1}(t) = &\frac{i}{2}\left[\sqrt{1+\sin\theta}\hat{a}^{\dagger}_{i10} + \sqrt{1-\sin\theta}\hat{a}^{\dagger}_{i20}\right]\sinh(\kappa\sqrt{1+\sin\theta}t) + \\
&+ \frac{1}{2}\left[\hat{a}_{s10} + \hat{a}_{s20}\right]\cosh(\kappa\sqrt{1+\sin\theta}t) + \\
&+ \frac{i}{2}\left[\sqrt{1-\sin\theta}\hat{a}^{\dagger}_{i10} - \sqrt{1+\sin\theta}\hat{a}^{\dagger}_{i20}\right]\sinh(\kappa\sqrt{1-\sin\theta}t) + \\
&+ \frac{1}{2}\left[\hat{a}_{s10} - \hat{a}_{s20}\right]\cosh(\kappa\sqrt{1-\sin\theta}t)
\end{aligned}
$$

$$
\begin{aligned}
\hat{a}_{s2}(t) = &\frac{i}{2}\left[\sqrt{1+\sin\theta}\hat{a}^{\dagger}_{i10} + \sqrt{1-\sin\theta}\hat{a}^{\dagger}_{i20}\right]\sinh(\kappa\sqrt{1+\sin\theta}t) + \\
&+ \frac{1}{2}\left[\hat{a}_{s10} + \hat{a}_{s20}\right]\cosh(\kappa\sqrt{1+\sin\theta}t) + \\
&- \frac{i}{2}\left[\sqrt{1-\sin\theta}\hat{a}^{\dagger}_{i10} - \sqrt{1+\sin\theta}\hat{a}^{\dagger}_{i20}\right]\sinh(\kappa\sqrt{1-\sin\theta}t) + \\
&- \frac{1}{2}\left[\hat{a}_{s10} - \hat{a}_{s20}\right]\cosh(\kappa\sqrt{1-\sin\theta}t)
\end{aligned}
\tag{3.4}
$$

When $\theta = \pi/2$ the idlers are shared (fully overlapping). In this case the idler and signal creation and annihilation operators reduce to

$$
\begin{aligned}
\hat{a}_{i}(t) &= \hat{a}_{i0}\cosh(\kappa\sqrt{2}t) + \frac{i}{\sqrt{2}}\left(\hat{a}^{\dagger}_{s10} + \hat{a}^{\dagger}_{s20}\right)\sinh(\kappa\sqrt{2}t) \\
\hat{a}_{s1}(t) &= \frac{1}{2}\left(\hat{a}_{s10} + \hat{a}_{s20}\right)\cosh(\kappa\sqrt{2}t) + \frac{\hat{a}_{s10} - \hat{a}_{s20}}{2} + \frac{i}{\sqrt{2}}\hat{a}^{\dagger}_{i0}\sinh(\kappa\sqrt{2}t) \\
\hat{a}_{s2}(t) &= \frac{1}{2}\left(\hat{a}_{s10} + \hat{a}_{s20}\right)\cosh(\kappa\sqrt{2}t) + \frac{\hat{a}_{s20} - \hat{a}_{s10}}{2} + \frac{i}{\sqrt{2}}\hat{a}^{\dagger}_{i0}\sinh(\kappa\sqrt{2}t)
\end{aligned}
\tag{3.5}
$$

Where we dropped the 1 in $\hat{a}_{i1}$ and $\hat{a}_{i10}$, since there is now only one idler. It is obvious that the two signals are indistinguishable, the two expressions are identical. Applying the number operator for the idler $\hat{n}_i = \hat{a}_i^\dagger \hat{a}_i$ to the vacuum state $|0_{s1}, 0_{s2}, 0_i\rangle$ produces

$$\hat{n}_i|0,0,n\rangle = \hat{a}_i^\dagger \hat{a}_i|0,0,n\rangle = (n\cosh^2(\kappa\sqrt{2}t)+1)|0,0,n\rangle + \\ + \frac{i}{\sqrt{2}}\sqrt{n+1}\sinh(\kappa\sqrt{2}t)\cosh(\kappa\sqrt{2}t)\left(|1,0,n+1\rangle + |0,1,n+1\rangle\right) \quad (3.6)$$

One can not know if an idler will be accompanied by a signal in path 1 or in path 2, so the two signals are actually in a single photon entangled state. One way to investigate the entanglement experimentally, in the ideal case of a completely shared idler as well as with varying degrees of overlap, would be to make interference measurements on the two signal beams.

Photon statistics

In order to calculate expectation values for the number of down-converted photons in the shared idler case ($\theta = \pi/2$) we use the solutions obtained in 3.5, and assume the initial states of both signal and idler to be the vacuum state $|vac\rangle = |0_{s1}, 0_{s2}, 0_i\rangle$. Recalling that $\hat{a}_m|vac\rangle = 0$ ($m = s1, s2, i$), and following the steps in 2.8, the expectation values for signal 1, signal 2 and idler follow.

$$\langle \hat{n}_i(t)\rangle = \sinh^2(\kappa\sqrt{2}t) \\ \langle \hat{n}_{s1}(t)\rangle = \frac{1}{2}\sinh^2(\kappa\sqrt{2}t) = \langle \hat{n}_{s2}(t)\rangle \quad (3.7)$$

Noticing here that the photon number expectation value corresponds to the photon flux in a SPDC process, the factor $\sqrt{2}$ showing up in expression 3.7, augmenting the coupling strength for the shared idler case with respect to the expression in eq. 2.8, affects the output intensity and thus the relative strength of different SPDC processes.

Phase correlations

To illustrate the phase correlations one can look at the quadrature operators $X = (\hat{a} + \hat{a}^\dagger)/\sqrt{2}$ and $Y = i(\hat{a} - \hat{a}^\dagger)/\sqrt{2}$. They are the real and imaginary components of the normalized complex field amplitude, and are thus measurable quantities. For the case of shared idler ($\theta = \pi/2$) we get the quadratures for the signal 1 as

$$X^{signal1} = \frac{1}{2\sqrt{2}}\left(\hat{a}_{s10} + \hat{a}_{s10}^\dagger + \hat{a}_{s20} + \hat{a}_{s20}^\dagger\right)\cosh(\kappa\sqrt{2}t) + \frac{\hat{a}_{s10} + \hat{a}_{s10}^\dagger - \hat{a}_{s20} - \hat{a}_{s20}^\dagger}{2\sqrt{2}} \\ + \frac{i}{2}\left(\hat{a}_{i0}^\dagger - \hat{a}_{i0}\right)\sinh(\kappa\sqrt{2}t)$$

$$Y^{signal1} = \frac{i}{2\sqrt{2}}\left(\hat{a}_{s10} - \hat{a}_{s10}^{\dagger} + \hat{a}_{s20} - \hat{a}_{s20}^{\dagger}\right)\cosh(\kappa\sqrt{2}t) + \frac{\hat{a}_{s10} - \hat{a}_{s10}^{\dagger} - \hat{a}_{s20} + \hat{a}_{s20}^{\dagger}}{2\sqrt{2}} - \frac{1}{2}\left(\hat{a}_{i0}^{\dagger} - \hat{a}_{i0}\right)\sinh(\kappa\sqrt{2}t)$$

The quadratures for signal 2 differ from the expressions for signal 1 only in the sense that the initial values of the two signals are interchanged, which does not affect the phase. The phases of signal 1 and signal 2 are completely correlated.

Chapter 4

Experimental realization

This chapter will report on the experimental realization of spontaneous parametric down-conversion in a two dimensional QPM structure. To investigate the phase correlations and entanglement properties of the down-converted light, one first needs to find a working point for the particular process of interest, i.e identify the correct frequencies and propagation directions of signal and idler, as well as the right experimental conditions to allow this particular process. Here, the process of particular interest is the shared idler SPDC. A periodically poled hexagonal lattice is used, and the focus is on finding the conditions that allow shared idler SPDC, and thus produce two correlated signal beams emitted symmetrically around the symmetry axis of the 2D lattice, as described in the end of section 2.

For applications in quantum communication, photons at telecommunication wavelengths around 1500 nm are convenient since optical fibers today are optimized for these frequencies. Similarly, many quantum detection schemes have high sensitivity around 800 nm, making these wavelengths interesting. In this work, the geometry of the QPM structure is chosen as to produce signals at 800-850 nm, and idlers at 1450-1550 nm, allowing e.g. coherent twin idlers to be transmitted through optical fibers, heralded by the detection of a signal. The crystal is pumped at 532 nm.

This chapter is structured in the following way. First, some of the expressions and relations derived in previous chapters will be expressed in terms of variables that can be controlled or measured experimentally. From this, numerical calculations allow an estimate of the working point, the frequencies and propagation directions of the signal and idler fields, as well as an estimate of the gain and efficiency of the processes. This is followed by a description of the experimental steps as well as the material and optics used in the measurement setup. In the end of this chapter the experimental results will be presented.

4.1 Properties of a 2D QPM system

To realize SPDC in a nonlinear crystal the system has to satisfy the conditions for momentum conservation in eq.2.2, to match the phases of the electromagnetic fields participating in the interaction and thereby permit the down-conversion process. In what follows QPM is achieved by 2D periodic poling to form a hexagonal lattice with period Λ, as illustrated in figure 2.3.

The coupled wave equations describe the evolution of signal and idler fields in classical electromagnetic theory. By normalizing the complex field amplitudes A_m according to $a_m = \sqrt{n_m/\omega_m}A_m$, as described in section 2.3, we can write out the normalized coupled wave equations, assuming monochromatic plane waves, as:

$$\begin{aligned} \frac{da_s(x)}{dx} &= -i\kappa a_i^*(x)\mathrm{e}^{-i\Delta kx} \\ \frac{da_i(x)}{dx} &= -i\kappa a_s^*(x)\mathrm{e}^{-i\Delta kx} \end{aligned} \tag{4.1}$$

where the no pump depletion approximation has been used, so that the pump field is assumed constant and has been incorporated in the coupling constant κ. The approximation is valid as long as the conversion efficiency is low, which will be true for low pump intensities. The coupling constant κ is given by

$$\kappa = 2\pi\sqrt{\frac{2\pi c}{n_s n_i n_p \lambda_s \lambda_i \lambda_p}}d_{eff}a_p(0) \tag{4.2}$$

The refractive indices of the nonlinear medium $n_m = n(\omega_m)$, for $m = p, s, i$, are frequency dependent. The constants μ_0 and ϵ_0 are the permeability and permittivity of vacuum and c is the speed of light in vacuum. The effective nonlinear optical coefficient d_{eff} depends on QPM lattice parameters, and can be found by considering the mathematical description of the lattice. As described in section 2.3, the spatially varying nonlinear susceptibility of the QPM structure can be expanded in a Fourier series. In a 2D lattice, the spatially varying nonlinear coefficient then takes the form

$$d(x, y) = d_{33}\sum_{l,m} F_{lm}\exp(i\mathbf{G}_{lm}\cdot\mathbf{r}) \tag{4.3}$$

The Fourier coefficients F_{lm} are determined by the geometry of the lattice, and the modification of d is dependent on the QPM orders l, m of the reciprocal lattice vectors $\mathbf{G}_{l,m}$ active in the SPDC process, as illustrated in fig. 2.3 and 2.4.

Inserting eq. 4.3 in the coupled wave equation leads to a new expression for momentum conservation, in vectorial form.

$$\Delta\mathbf{k}_{eff} = \mathbf{k}_p - \mathbf{k}_s - \mathbf{k}_i - \mathbf{G}_{l,m} = 0 \tag{4.4}$$

Where $\mathbf{k}_{eff}$ is the effective momentum mismatch. In the following we will be working with the lowest order RLVs, namely $\mathbf{G}_{1,0}$ and $\mathbf{G}_{0,1}$, from now on referred to as $\mathbf{G}_1$ and $\mathbf{G}_2$ respectively. The magnitude of $\mathbf{G}_1$ and $\mathbf{G}_2$ is $|\mathbf{G}| = 4\pi/\sqrt{3}\Lambda$. The grating period is chosen to be $\Lambda = 8.3\mu$m to allow for production of signal and idler at the wanted wavelengths, and the duty cycle $D = 50\%$ describes the relative size of the motif and the grating period as depicted in figure 4.1. As mentioned above, the nonlinear coefficient that will be used is d_{33}, which is valid for vertical (z) polarization of all three pump, signal and idler fields. The effective nonlinear coefficient for a hexagonal lattice, using the lowest order RLVs and 50% duty cycle, is $d_{eff} = F_{1,0}d_{33} = F_{0,1}d_{33} = 0.29d_{33}$ [22].

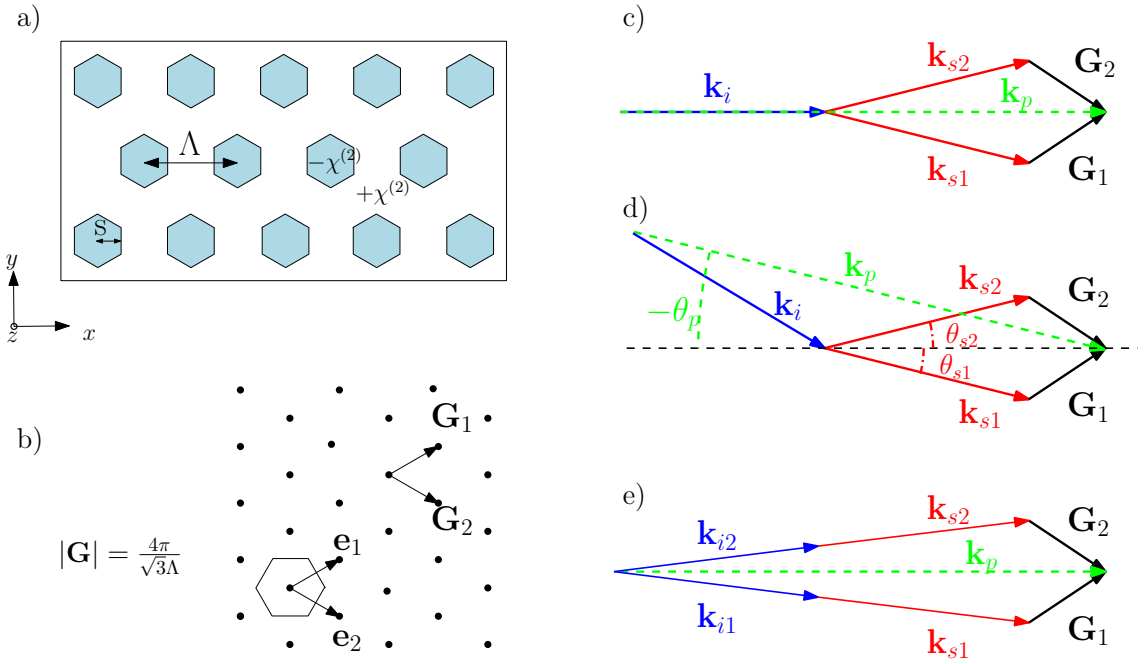

Figure 4.1: a) $\chi^{(2)}$ domain inverted 2D grating of period Λ, where the parameter s gives the duty cycle $D = 2s/\Lambda$. b) The reciprocal QPM lattice with RLVs $\mathbf{G}_{1,0}$ and $\mathbf{G}_{0,1}$. The hexagon at the bottom represents the standard 1^{st} Brillouin zone. To the right, momentum conservation illustrated by closing the wavevector diagram in the reciprocal QPM lattice. The RLVs $\mathbf{G}_1 = \mathbf{G}_{1,0}$ and $\mathbf{G}_2 = \mathbf{G}_{0,1}$ make up for the momentum mismatch $\Delta\mathbf{k}$. c) Shared idler SPDC in the symmetric case, $\theta_p = 0°$. d) Shared idler SPDC in a non-symmetric case, i.e. $\theta_p \neq 0°$. e) Two uncoupled SPDC processes, in the symmetric case, with idler and signal colinear.

4.2 A numerical model for 2D SPDC

The purpose of the numerical analysis is to gather insights on the device response and design accordingly the experimental setup, and investigate the impact of experimental control parameters - such as pump incidence angle, sample temperature and pump power - on the signal an idler properties. The numerical model provides guidelines for the experiments by predicting the wavelengths and propagation angles of signal and idler, which simplifies the experimental procedure as well as the analysis of the measurement results.

The numerical model is based on the vectorial condition for momentum conservation in eq. 4.4, as well as the electric field amplitudes and the coupling constant κ from eq. 4.2. The Sellmeier equations as reported in [23] were used to calculate the refractive index dispersion of the material.

4.2.1 Spectral angular response

The spectral angular response, that is the complete set of signal and idler field frequencies and output angles from the SPDC process, is calculated from the two scalar components of the vectorial QPM condition for momentum conservation in

eq. 4.4, given the properties of our QPM crystal. It provides the working point in terms of signal and idler wavelengths and output angles, for any particular process that we are interested in.

In figure 4.2 the idler propagation angle is plotted against the idler wavelength, and the signal propagation angle against the signal wavelength. Blue and red curves imply quasi phase matching processes using the reciprocal lattice vectors $\mathbf{G}_1$ and $\mathbf{G}_2$ respectively.

All propagation angles are defined in relation to the lattice symmetry axis so that $\theta_{sym} = 0°$. The angles given in the plots are internal to the crystal, i.e the actual measured angles will be larger by a factor of the refractive index n_m, for $m = p, s, i$, according to Snell's law. For the crystal used here the refractive indices are $n_m \simeq 2.15$. The sample temperature is set to 80°C.

The situation when the pump propagates along the lattice symmetry axis so that $\theta_p = 0°$ will be referred to as the symmetric case. In the symmetric case the shared idler will be collinear with the pump, and the twin signal beams will be emitted symmetrically on each side of the pump (and idler) beam. The twin signals are *always* emitted symmetrically around the lattice symmetry axis, but with different propagation angles depending on the wavelength.

According to figure 4.2 the shared idler (SI) wavelength is in the symmetrical case $\lambda_i^{SI} = 1444$ nm. From energy conservation, $\omega_p = \omega_s + \omega_i$, it follows that the wavelength of the twin signals is $\lambda_s^{SI} = 842$ nm. The internal propagation angles for the twin signal beams are $\theta_s^{SI} \pm 1.6°$, which translate into $\theta_s^{SI,external} \simeq \pm 3.4°$ after exiting the crystal ($n_s \simeq 2.15$). In the symmetric case we expect also a shared signal (SS) at $\lambda_s^{SS} = 833$ nm, with twin idlers at $\lambda_i^{SS} = 1472$ nm. The focus in the experimental part will be on tracking the twin signals expected at 842 nm, coupled through the shared idler at 1444 nm, since finding the working point for this process would allow us to design a measurement scheme for quantum phase and entanglement measurements. It will also directly allow us to qualitatively investigate the expected gain enhancement of the SI and SS processes.

4.2.2 Efficiency

Assuming momentum conservation, the coupled wave equations in eq. 4.1 reduce to the same form as the quantum mechanical equations of motion 3.2 for $\theta = 0$. Consequently, the solutions are on the same form as well, and we exploit this fact to get an expression for the signal and idler output intensities. For a crystal length L, the signal and idler normalized field amplitudes can then be written (from 3.4)

$$a_s(L) = ia_{i0}^* \sinh(\kappa L) + a_{s0} \cosh(\kappa L)$$
$$a_i(L) = a_{i0} \cosh(\kappa L) + ia_{s0}^* \sinh(\kappa L)$$

The photon flux ϕ_s of signal photons is then given by the expression below. In the limit of large gains $\kappa L \gg 1$, the flux of signal photons grows exponentially with κL.

$$\phi_s \propto |a_s(L)|^2 = |a_{i0}|^2 \sinh^2(\kappa L) + |a_{s0}|^2 \cosh^2(\kappa L) \xrightarrow{\kappa L \gg 1} \frac{|a_{i0}|^2 + |a_{s0}|^2}{4} e^{2\kappa L}$$

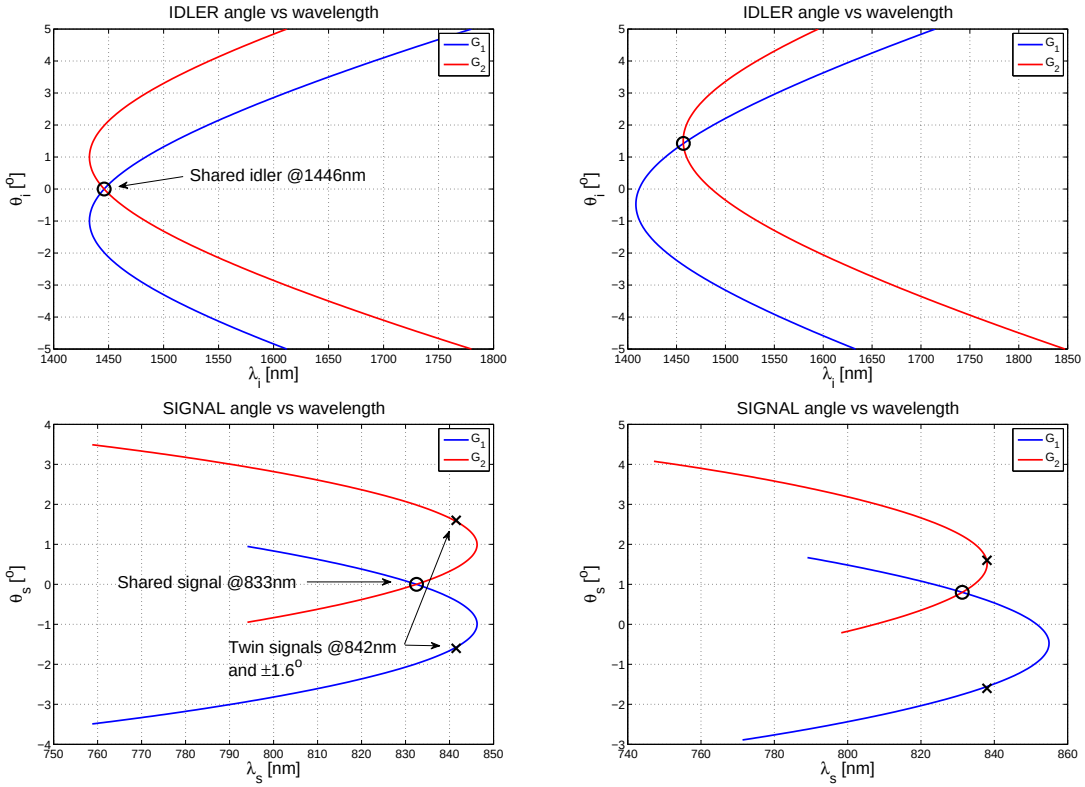

Figure 4.2: Numerical calculations from QPM conditions. Plots show the relation between wavelength and propagation angle for the idler (top) and the signal (bottom), for pump angle $\theta_p = 0°$ (left) and $\theta_p = 0.5°$ (right) in relation to the lattice symmetry axis. $T = 80°$ and $\Lambda = 8.3\mu m$. Sellmeyer eq. from [**?**].

For low gains the growth is quadratic in κL. The signal intensity at the output in the exponential gain regime can be calculated from the following expression.

$$I_s = \frac{1}{2}\sqrt{\frac{\epsilon_0}{\mu_0}}\omega_s|a_s(L)|^2 \simeq \frac{1}{2}\sqrt{\frac{\epsilon_0}{\mu_0}}\omega_s\frac{|a_{i0}|^2+|a_{s0}|^2}{4}e^{2\kappa L} \tag{4.5}$$

where the normalized field amplitude a_{m0}, $m = i, s$, relates to the input intensity I_{m0} through

$$a_{m0} = \sqrt{\frac{2}{\omega_m}\sqrt{\frac{\mu_0}{\epsilon_0}}I_{m0}}$$

Following this, calculations of the gain coefficient κL and simulations of the expected output power of signal and idler were performed, with the parameters of the experimental setup (details in section 4.3.3). To reach the exponential gain regime the gain coefficient κL should be significantly larger than 1. The gain parameter can be expressed in terms of measurable quantities:

$$\kappa L = 2\pi\sqrt{\frac{2}{n_s n_i \lambda_s \lambda_i}\sqrt{\frac{\mu_0}{\epsilon_0}}I_p(0)}d_{eff}L \gg 1 \tag{4.6}$$

Inserting in equation 4.6 the parameter values of our experimental setup, described in detail in the next section, the theoretical gain coefficient can be calculated, and is found to be well above the limit for exponential growth, namely $\kappa L \simeq 40$ pV/m. For the particular frequencies of interest, and the QPM lattice properties of the crystal used here, reaching the exponential gain regime corresponds to reaching a continuous wave (CW) pump power satisfying $I_p^{CW} \gg 50$ W. This implies that a pulsed laser is needed to obtain high conversion rates.

The conclusion to draw from these calculations, considering the relatively high value of the theoretical gain parameter, is that the damage threshold of the crystal, rather than the laser power available, will be critical for reaching the regime of efficient down-conversion. Even though the crystal chosen for this work has relatively high optical damage threshold, this is always a limiting factor. Details on the measurement conditions are presented in section 4.3.

Since the signal and idler input powers originate from vacuum fluctuations, a more rigorous model would be needed to predict output powers more precisely. Here, the aim of the simulations is to give a clue on the order of magnitude of the power output.

4.3 Experimental Procedure

The focus of the measurements was on identifying the experimental working points corresponding to the generation of twin signal beams at wavelength λ_s^{SI}, quasi phase matched by the $\mathbf{G}_1$ and $\mathbf{G}_2$ RLVs and coupled by a shared idler at λ_i^{SI}, and verifying the predictions of section 3, in particular the gain enhancement for shared idler (signal) processes. The spectral angular response calculated above was used as a guideline for the experimental investigations.

4.3.1 The nonlinear crystal

The QPM lattice used in the SPDC measurements is made on a z-cut stoichiometric $LiTaO_3$ substrate, doped with 1 mol% MgO and periodically poled to form a hexagonal 2D structure as in fig.4.1 (hexMgSLT, Oxide Corp.). The sample is 20 mm long (x direction), 4 mm wide (y) and 0.5 mm thick (z), and the QPM period is $\Lambda = 8.3$ μm.

Several factors motivated the use of MgSLT for the 2D QPM structure, notably the high second-order nonlinearity [24], high optical damage threshold and thermal conductivity [25], which allow for higher pumping. Also, the large transparency range $LiTaO_3$ (280-5500 nm) makes $LiTaO_3$ interesting for a large spectrum of nonlinear optics applications.

The QPM period Λ was chosen as to get the signal wavelength around λ_s =800 nm and idlers at λ_i =1500 nm.

4.3.2 Laser properties and Damage threshold

The QPM crystal was pumped with a pulsed Nd:YAG laser (Litron lasers, Nano T series) with an additional frequency doubling crystal converting its output from 1064 nm to 532 nm. See table 4.1 for details. Incorporated in the laser system is an adjustable attenuator transmitting 10-100% of the laser light.

Wavelength	Pulse energy	Rep. rate	Pulse duration	Peak power
532 nm	60 mJ	20 Hz	10 ns	6 MW

Table 4.1: Nd:YAG, Litron Nano T, properties

The literature can not provide a clear answer on the damage threshold for the hexMgSLT crystal, since it depends on many factors: the state of the crystal surfaces, focusing conditions, laser properties such as peak and average powers, pulse duration and wavelength. However, some clues can be found e.g. in a paper by Kitamura et al. [26] where MgSLT is shown to cope a peak power density of 0.57 GW/cm^2 when pumped at 1064 nm with a 9 ns, 30 Hz pulsed laser, which is similar to the laser used here. Damage threshold generally scales with wavelength [27], inferring that a peak power density of 0.28 GW/cm^2 at 532 nm would be tolerable for the MgSLT crystal.

The starting point here was to stay within a reasonable margin to this value. In the measurements producing the results presented here, the pump peak power was

0.07 MW. The beam diameter at the laser output was 4 mm, and it was focused using a f = 500 mm spherical lens to produce a beam spot with a 1/e-diameter of $D = 85\mu$m in the crystal, according to theoretical estimates. The peak power density was then reaching a theoretical maximum of 1.3 GW/cm^2.

4.3.3 Setup

The experimental setup for the measurements producing the results in section 4.4, was as in figure 4.3.

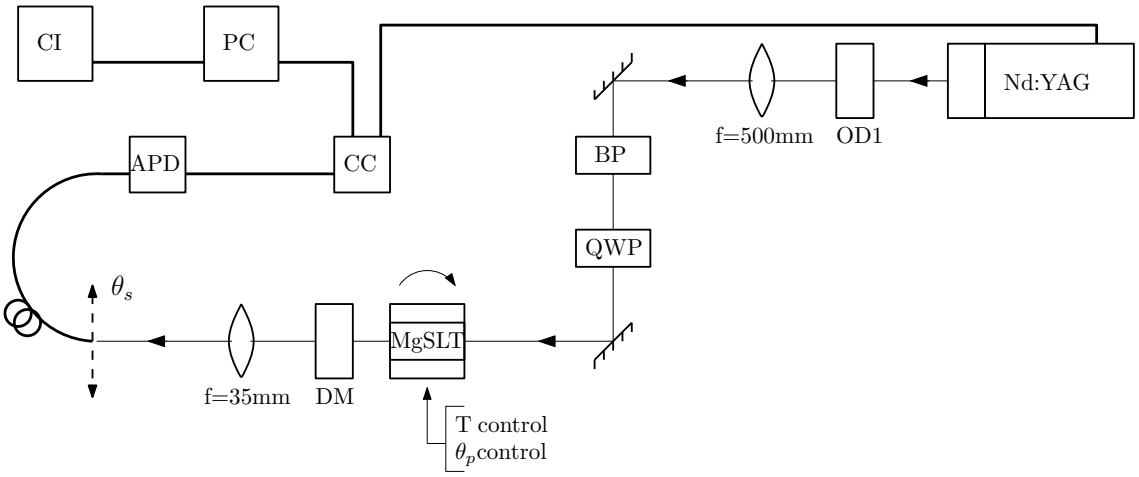

Figure 4.3: The experimental setup. The pump is filtered through OD1= optical density filter and BP=bandpass filter at 532±3 nm, polarization change with QWP=quarter wave plate, temperature control and pump angle control in the crystal mount, coupling into fiber on translational stage, detection by ADP=avalanche photo diodes, dark counts removed by CC=coincidence counter. PC=photon counter, CI=computer interface.

The pump power was reduced with a neutral density filter (OD1), and unwanted frequencies in the pump filtered out by a band pass filter transmitting at 532±3 nm (some lasers have excess light at wavelengths around 800-850 nm, same as the expected signals here). The originally horizontally polarized pump beam was passing through a quarter wave plate to obtain circularly polarized light. The $d_{33} \simeq 17$ pV/m, which is the largest of the nonlinear optical coefficients for MgSLT, is exploited when using vertically polarized light (we didn't have a half wave plate in the lab, so we basically only made use of half of the pump power). Vertical and horizontal positioning of the beam is controlled by the two metallic mirrors. The crystal is placed on a copper oven, controlled by two Pelletier elements connected to a temperature controller. The oven is mounted on an xyz micropositioning stage, allowing micrometer control in the vertical and horizontal direction, as well as fine angular adjustments in the horizontal plane.

After the crystal, the pump was rejected by a dichroic mirror, while the transmitted light was focused by a f=35 mm spherical lens located one focal distance away from the crystal. The signal output was then collected with a fiber in the Fourier plane of the output focusing lens. The fiber was mounted on a translational

stage, allowing translation in both x, y and z direction with 10-micrometer control. After trying a few different configurations we settled for free space coupling, using a multimode fiber with a 62.5 μm core.

The detection was done with silicon avalanche photo diodes (APD), with efficiency of 55% at $\lambda = 830$ nm. Since the responsivity of the APD is restricted to the 400-1000 nm range, only the signals could be detected. The APD recovery time of 30 ns is longer than the pulse length of 10 ns, i.e it can only detect one photon per pulse, resulting in a maximum possible count rate of 20 counts per second, following the pump repetition rate is 20 Hz. Connected to the APDs is a monochromator, remote controlled from a computer interface, allowing to choose frequencies and scan over a large spectrum.

To reduce noise a coincidence counter was inserted between the APD and the photon counter. The coincidence is made between the detected photons and the electric signal from the laser system, announcing the departure of a pump photon. Only letting through the detected photons matching a signal from the laser reduces dark counts to virtually zero ($p_{dark} < 10^{-6}$). A delay generator was used to adjust for the time delay originating from the departure time difference of pump photon vs laser system, and the difference in path lengths.

4.3.4 Measurement

A first experimental attempt was made with a small 50 mW CW laser at 532 nm. Although no conversion could be detected, it allowed optimization of the optical path; focusing, filtering and fiber coupling. For the final experiments and the results presented below, a pulsed Nd:YAG laser at wavelength $\lambda_p = 532$ nm was used. Detection was first made with a semiconductor detector (Newport Power Meter). However, the short, low frequency laser pulses could not be properly registered by the detector, so the data for the results presented in section 4.4 was collected using avalanche photo diodes.

With everything in place and aligned, the sample was positioned on the stage and heated to 80°C. The laser power was adjusted to a suitable value - 10^3 attenuation of the maximum pump power in the beginning (see table 4.1). The spectral response is very sensitive to changes in the pump incidence angle, so finding the symmetric position, i.e pump collinear with the lattice symmetry axis, is not a straightforward task. To overcome this challenge and achieve correct angular positioning of the crystal, we made use of the fact that in the symmetric case the shared signal (SS) also propagates along the lattice symmetry axis. By measuring the spectrum in the pump propagation direction, for different values of θ_p as shown in figure 4.4, and identifying the SPDC signal output, close to symmetric positioning could be achieved. At $\theta_p = 0°$, the shared signal should be collinear with the pump, which can be seen in figure 4.4 where $\lambda_s^{SS} = 830$ nm (black). For larger pump angles the shared signal is no longer collinear with the pump, but we can instead see two signals separated in wavelength, shown here for $\theta_p = 1°$ (blue) and $\theta_p = 2°$ (red) external (measured) angle. In the spectral-angular response plots the pump angle is marked in red. This is where the spectra are measured. Figure 4.4 also allows us to calculate the offset in frequency of the numerical model against reality, by reading

off the difference between the predicted value of the shared signal $\lambda^{SS}_{theory} = 833$ nm and the measured peak centered at $\lambda^{SS}_{exp} = 830.5$ nm. This result is useful in the following to find the working points for particular processes.

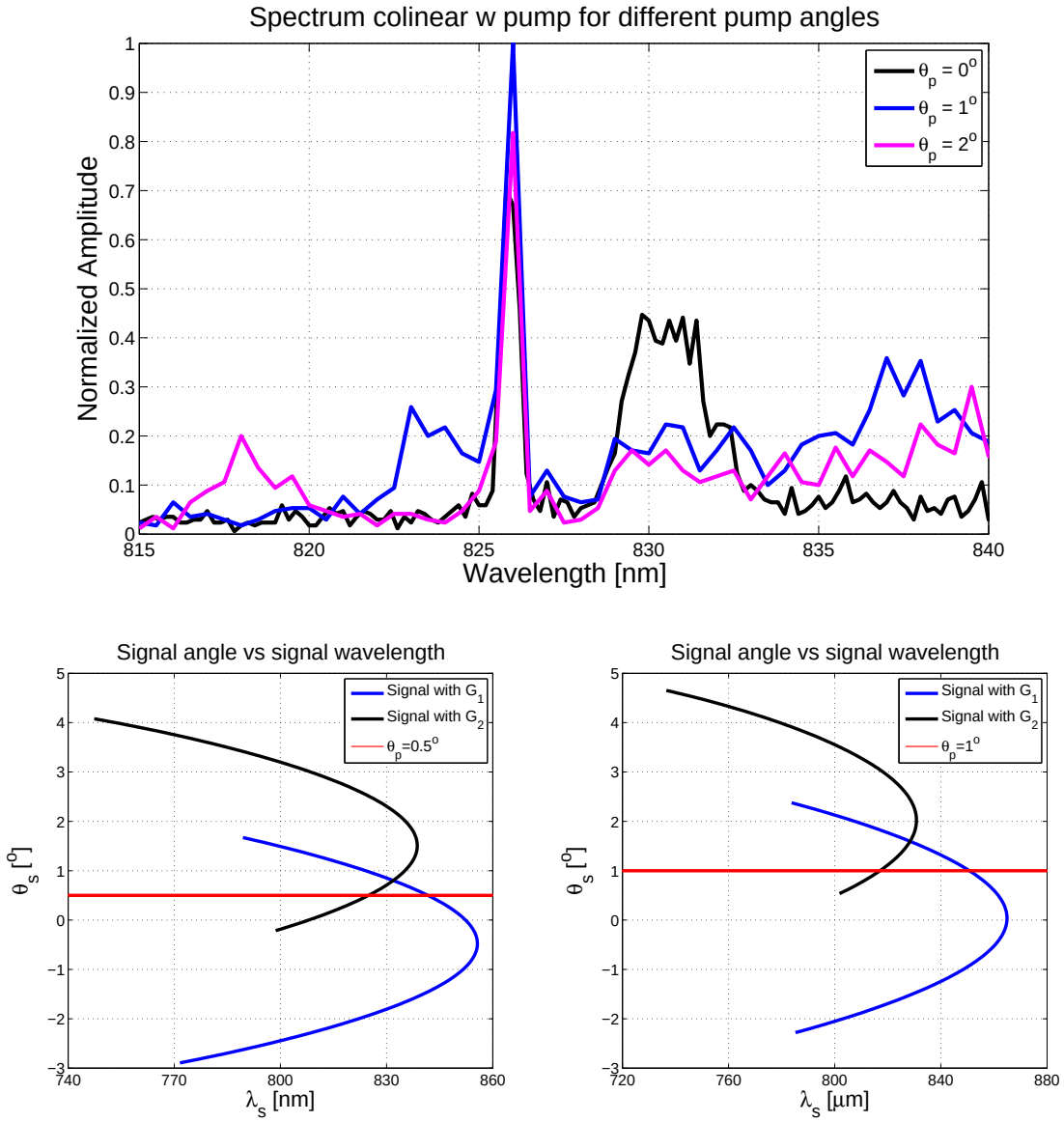

Figure 4.4: Spectrum measured in the propagation direction of the pump for $\theta_p \simeq 0°$ (black), $\theta_p \simeq 1°$ (blue) and $\theta_p \simeq 2$ (magenta) *external* angles (the spectral-angular plots show *internal* angles). Since the SS and SI are always collinear with the crystal axis, but only collinear with the pump in the symmetric case, this allows very close to correct positioning of the crystal in relation to the pump.

After identifying the symmetric position, the strategy was to find the working point for generation of twin signal beams, coupled by a shared idler, with the help of the numerical predictions of wavelengths and propagation angles from section 4.2.1.

4.4 Experimental results

The twin signal beams in the symmetric case, $\theta_p = 0$, are shown in figure 4.5. They were measured at external angles $\pm 3.4°$ and the peaks are centered at wavelength $\lambda_{s1}^{SI} = 840$ nm and $\lambda_{s2}^{SI} = 840.5$ nm respectively. The bandwidths of both are $\Delta \simeq 1$ nm (FWHM). The twin beams should of course be centered at the same wavelength if they are coupled to the same idler. The origin of the frequency shift is not known, but a plausible reason is temperature fluctuations, changing the spectral-angular response between the two measurements. The maximum temperature fluctuations measured were $\pm 1.8°$C, which corresponds to wavelength fluctuations of ± 0.6 nm. Since an infinite number of signal wavelengths are actually produced, with a continuous spread in propagation angle, the frequency shift can also be the result of the measurements being taken slightly off the main propagation axis of the SI signals.

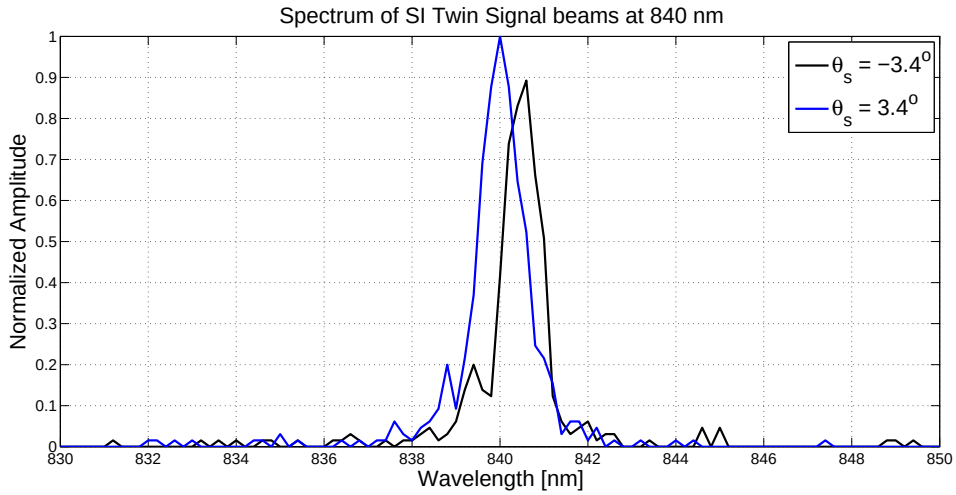

Figure 4.5: The symmetric case $\theta_p \simeq 0°$: The SI (shared idler) twin signal peaks centered at $\lambda_s^{SI} = 840$ and 840.5 nm, at external angles $\theta_s^{SI} \simeq \pm 3.4°$. The bandwidths of the peaks are 1.0 and 1.1 nm respectively (FWHM). The λ-shift between the two peaks probably originates in temperature fluctuations or slightly off-axis measurements.

The experimental results support the conclusion from analytic derivations in section 3 that the amplitudes are at a maximum for the coupled shared idler/signal SPDC processes. However, the reality is not as simple as the model, but some processes, among them the SS/SI processes, were enhanced, and some were not seen at all. High conversion was found mainly at the higher end of allowed signal wavelengths (in the curved end of the spectral-angular response plots in fig 4.2), and at the central SI/SS area. One example of a strong peak is the case where $\theta_i = \theta_s$, i.e when signal and idler are collinear, the case which is shown in figure 4.7. More extensive analytic and numeric models are needed to get a more realistic overview of the spectral response.

The shared signal, shown in figure 4.6, was centered at $\lambda_s^{SS} = 830.5$ nm, but the bandwidth is quite large, ~ 4 nm in the symmetric case ($\theta_p \simeq 0°$), and was slightly disturbed by noise originating from the pump.

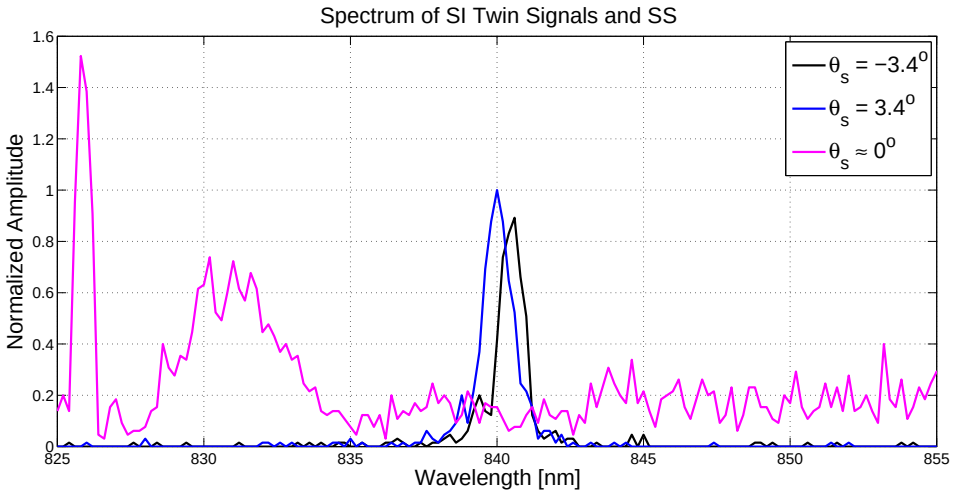

Figure 4.6: The symmetric case $\theta_p \simeq 0°$: SI twin signals centered at $\lambda_s^{SI} = 840$ and 840.5 nm at external angles $\theta_s^{SI} \simeq \pm 3.4°$, and the shared signal (SS) peak centered at $\lambda_s^{SS} = 831$ nm and $\theta_s^{SS} \simeq 0°$. The SS spectra is collected slightly off the pump propagation direction, for noise reduction reasons, resulting in a slightly lower count rate and, possibly, broadened spectrum.

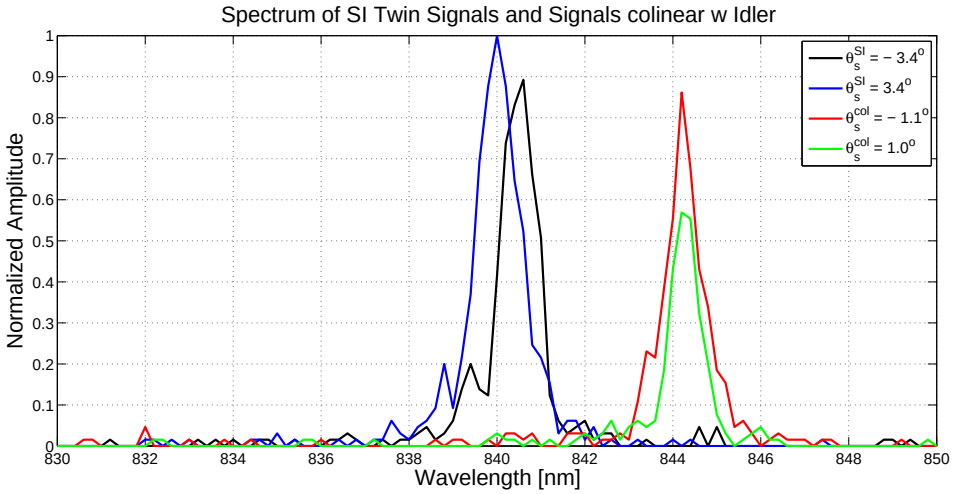

Figure 4.7: The symmetric case $\theta_p \simeq 0°$: SI twin signals at wavelength $\lambda_s^{SI} \simeq 840$ nm and external angle $\theta_s^{SI} \simeq \pm 3.4°$, and in the case where signal and idler are collinear, found at $\lambda_s^{coll} = 844$ nm and external angle $\theta_s^{coll} \simeq 1°$. The signal/idler collinear process also shows enhancement in relation to random SPDC processes, but are slightly weaker than the SI processes.

The results from the measurements are in general in good compliance with the numerical model, with only slight shifts in wavelengths.

Chapter 5

Discussion

The experiments were successful, the experimental working points allowing the generation of twin signals were found, and critical aspects were identified and analyzed to enable further improvement of the measurement setup and process. The gain enhancement of the coupled processes was clearly visible, together with certain other processes. A multimode numerical treatment of the problem could provide greater insight into the relative strength of concurrent processes.

We have a working numerical model that can be used to predict the spectral-angular response in 2D QPM experiments. The slight shift in wavelength between the measured peaks and the numerical model is a common phenomenon which relates to uncertainties in the Sellmeier equations. Deviations might also originate in temperature fluctuations, since the temperature control was not stable. The biggest measured deviations were $\pm 1.8°$C, corresponding to shifts in the spectral response of ± 0.6 nm. In addition, the difficulty of determining the pump angle in relation to the lattice symmetry axis resulted in an estimated uncertainty of $\pm 0.1°$ on the pump incidence angle. Measurement abnormalities also arise from the coupling optics. The down-converted light is emitted not from a point source but from a finite volume, which complicates the coupling and adds to the spectral and angular broadening of the measured peaks. Fiber alignment is critical to obtain a correct representation of the response, and it is a factor that can be further optimized for future measurements.

A large peak at $\lambda = 826$ nm was found in several of the spectra collected in the direction of pump propagation. This peak is not a product of SPDC (confirmed by two independent checks: changing to horizontal polarization and bringing the crystal out of the optical path), and it might be an excess product from the pump source. In a very narrow angular range around the pump propagation direction, a lot of noise in the frequency range $\lambda > 826$ nm was also observed. The level of the noise varied during the measurement process and might have its origin in interactions between the pump and the detection system, but it can not be verified at this time. This noise might play a role in the broadening of the shared signal, which points at the critical role of the choice of source for the experiments. The large SS bandwidth could also be explained by the uncertainty in pump angle, implying the measured SS peak is in fact two signals only partially overlapping, creating a broader peak. This could relatively easily be investigated experimentally with further measurements.

The fact that the crystal could cope with higher power densities than predicted - 1.3 GW/cm^2 without any visible damage - is promising for future applications using MgSLT.

According to the theoretical model, the phases of the twin beams are entirely correlated, and anticorrelated to the idler 3.5. Investigating this experimentally through phase measurements (e.g. interferometry) would be a natural continuation of this work. Partially, it has already been done by Jin et al., described in their paper from July 2013 [17]. However, the non-degenerate case, as the one considered in this thesis with signals/idlers at 800/1500 nm, has not been covered, and there remains a lot of interesting questions to be answered.

To exploit the possibilities of 2D QPM structures, a more extensive characterization of the spectral-angular response is suggested, both numerically and experimentally. The bandwidths found here should be checked against theoretical predictions (beyond the scope of the model described here), to assess the possibilities of further narrowing of the bandwidths. A few changes and optimization of the setup and detection systems would enable an estimate of the conversion efficiency of the SPDC process. The photon collection and detector setup used for this work did not allow appropriate efficiency measurements.

The quantum mechanical model derived in chapter 3 allows analysis of the SPDC process for varying degrees of overlap of two idlers or signals. A deeper insight into this would be interesting as it could provide means for controlling the degree of entanglement between two signal or idler modes. Further development of the model could allow us to explore the possibilities of entanglement in different degrees of freedom, and possibly forming a strategy for multi-photon state production with 2D SPDC. Also, a multimode treatment of the problem could be of interest. Furthermore, investigating whether correlated phases also entails correlated phase noise, could lead the way for e.g interferometry noise reduction.

Besides quantum optics applications, the phase correlations can find interesting applications in classical optics, as it provides a source for two entirely phase correlated beams, today achieved by phase modulators and interferometric systems [28].

Chapter 6

Summary and Conclusions

This is a study of the properties of light produced by spontaneous parametric down-conversion (SPDC) in a two-dimensional nonlinear lattice. The focus is on the quantum mechanical properties of the down-converted light, and the coupling between several electromagnetic modes. The products of SPDC, referred to as signal and idler, can be quantum entangled in multiple domains (frequency, polarization etc.), and 1D QPM structures are popular as entangled photon pair sources for quantum optics applications.

In this work, a quantum mechanical model is formulated for SPDC processes in a 2D QPM lattice. The model is then solved for the general case, and analyzed for the particular case when two modes overlap, i.e. when two SPDC processes are degenerate in idler frequency and spatial propagation direction. As a result, two signal modes are coupled through the shared idler, generating a twin beam signal output symmetrically around the lattice symmetry axis. To investigate the shared idler process in a physical system, measurements were made on a hexagonally poled $LiTaO_3$ crystal. A numerical model of 2D SPDC was built preceding the measurements, to predict the spectral-angular response and efficiency, and provide guidelines for the experimental setup.

According to the analytic model, signals coupled through a shared idler are correlated in phase and amplitude, and they form a single photon entangled state. In addition, the gain coefficient of the coupled processes is larger by a factor $\sqrt{2}$ compared to uncoupled processes, which was qualitatively confirmed in the measurements showing enhanced intensities for the shared idler (and shared signal) modes.

Possible continuations of this work includes experimentally investigating the phase correlations, and more extensively characterize the spectral-angular response of the 2D QPM crystal. Also, further development and analysis of the quantum mechanical model is suggested, to map correlations and different types of entanglement produced by SPDC in 2D QPM lattices.

Bibliography

[1] J.S. Bell, Physics **1**, 195 (1964).

[2] P.G. Kwiat, E. Waks, A.G. White, I. Appelbaum, P.H. Eberhard, Phys. Rev. A. **60**, R773 (1999).

[3] T. Nagata, R. Okamoto, J.L. OâĂŹBrien, K. Sasaki, and S. Takeuchi, Science **316**, 726 (2007).

[4] J.W. Pan, Z.B. Chen, C.Y. Lu, H.Weinfurter, A. Zeilinger, and M. Zukowski, Rev. Mod. Phys. **84**, 777 (2012).

[5] I. Usmani, C. Clausen, F. Bussie'res, N. Sangouard, M. Afzelius, and N. Gisin, Nat. Photonics **6**, 234 (2012).

[6] G. Bj ork, A. Laghaout, and U.L. Andersen, Phys. Rev. A **85**, 022316 (2012).

[7] J.C.F. Matthews, A. Politi, A. Stefanov, and J.L. OâĂŹBrien, Nat. Photonics **3**, 346 (2009).

[8] A. Politi, J.C.F. Matthews, and J.L. OâĂŹBrien, Science **325**, 1221 (2009).

[9] L. Sansoni, F. Sciarrino, G. Vallone, P. Mataloni, A. Crespi, R. Ramponi, and R. Osellame, Phys. Rev. Lett. **105**, 200503 (2010).

[10] J.A. Armstrong, N. Bloembergen, J. Ducuing, and P.S. Pershan, Phys. Rev. **127**, 1918 (1962).

[11] M. Yamada, N. Nada, M. Saitoh, and K. Watanabe, Appl. Phys. Lett. 62, **435** (1993).

[12] L.A. Eyres, P.J. Tourreau, T.J. Pinguet, C.B. Ebert, J.S. Harris, M.M. Fejer, L. Becouarn, B. Gerard, and E. Lallier, Appl. Phys. Lett. 79, 904 (2001).

[13] C. Langrock, S. Kumar, J.E. McGeehan, A.E. Willner, M.M. Fejer, Lightwave Technol. **24**, 2579 (2006).

[14] S. Tanzilli, W. Tittel, H. De Riedmatten, H. Zbinden, P. Baldi, M. De Micheli, D.B Ostrowsky, and N. Gisin, Europ. Phys. J. **D 18**, 155 (2002).

[15] V. Berger, Phys. Rev. Lett. **81**, 4136 (1998).

[16] K. Gallo, M. Levenius, F. Laurell, and V. Pasiskevicius, Appl. Phys. Lett. **98**, 161113 (2011).

[17] H. Jin, P. Xu, X.W. Luo, H.Y. Leng, Y.X. Gong, and S. N. Phys. Rev. Lett. **111**, 023603 (2013).

[18] H.-C. Liu and A.H. Kung, Opt. Express **16**, 9714 (2008).

[19] A. Yariv, *Optical Electronics in Modern Communications, 5th ed.* (Oxford University Press, New York, 1997), p. 305.

[20] L. Mandel, E. Wolf, *Optical Coherence and Quantum Optics* (Cambridge University Press, Cambridge, 1995), p. 1074.

[21] D.A. Kleinman, Phys. Rev. **174**, 1027 (1968).

[22] A. Arie, N. Habshoosh and A. Bahabad, Optical and Quantum Electronics **39**, 361 (2007).

[23] H.H. Lim, S. Kurimura, T. Katagai, and I. Shoji, Jpn. J. Appl. Phys.52(3R), 032601 (2013).

[24] N.E. Yu, S. Kurimura, Y. Nomura, and K. Kitamura, Jpn. J. Appl. Phys. **43**(10A), L1265 (2004).

[25] M. Nakamura, S. Takekawa, K. Terabe, K. Kitamura, T.Usami, K. Nakamura, H. Ito and Y. Furukawa, Ferroelectrics **273**, 199 (2002).

[26] N.E. Yu, S. Kurimura, Y. Nomura, K. Kitamura, Jpn. J. Appl. Phys. **43** L1265 (2004).

[27] "Laser Damage Threshold", Newport corp., https://www.newport.com/Laser-Damage-Threshold/144932/1033/content.aspx, April 2014.

[28] P.J. Clarke, R.J. Collins, V. Dunjko, E. Andersson, J. Jeffers, G.S. Buller, Nat. Commun. **3**, 1174 (2012).